



# Incidence and survival of remnant disks around main-sequence stars

H.J. Habing<sup>1</sup>, C. Dominik<sup>1</sup>, M. Jourdain de Muizon<sup>2,3</sup>, R.J. Laureijs<sup>4</sup>, M.F. Kessler<sup>4</sup>, K. Leech<sup>4</sup>, L. Metcalfe<sup>4</sup>, A. Salama<sup>4</sup>, R. Siebenmorgen<sup>4</sup>, N. Trams<sup>4</sup>, and P. Bouchet<sup>5</sup>

<sup>1</sup> Sterrewacht, Leiden, P.O. Box 9513, NL-2300 RA Leiden, The Netherlands

<sup>2</sup> DESPA, Observatoire de Paris, F-92190 Meudon, France

<sup>3</sup> LAEFF-INTA, ESA Vilspa, PO Box 50727, 28080 E-Madrid, Spain

<sup>4</sup> ISO Data Center, Astrophysics Division of ESA, Vilspa, PO Box 50727, E-28080 Madrid, Spain

<sup>5</sup> Cerro Tololo Inter-American Observatory, NOAO, Casilla 603, La Serena, Chile 1353

Received: ; accepted:

**Abstract.** We present photometric ISO 60 and 170  $\mu\text{m}$  measurements, complemented by some IRAS data at 60  $\mu\text{m}$ , of a sample of 84 nearby main-sequence stars of spectral class A, F, G and K in order to determine the incidence of dust disks around such main-sequence stars. Fifty stars were detected at 60  $\mu\text{m}$ ; 36 of these emit a flux expected from their photosphere while 14 emit significantly more. The excess emission we attribute to a circumstellar disk like the ones around Vega and  $\beta$  Pictoris. Thirty four stars were not detected at all; the expected photospheric flux, however, is so close to the detection limit that the stars cannot have an excess stronger than the photospheric flux density at 60  $\mu\text{m}$ .

Of the stars younger than 400 Myr one in two has a disk; for the older stars this is true for only one in ten. We conclude that most stars arrive on the main sequence surrounded by a disk; this disk then decays in about 400 Myr. Because (i) the dust particles disappear and must be replenished on a much shorter time scale and (ii) the collision of planetesimals is a good source of new dust, we suggest that the rapid decay of the disks is caused by the destruction and escape of planetesimals. We suggest that the dissipation of the disk is related to the heavy bombardment phase in our Solar System. Whether *all* stars arrive on the main sequence surrounded by a disk cannot be established: some very young stars do not have a disk. And not all stars destroy their disk in a similar way: some stars as old as the Sun still have significant disks.

**Key words:** Stars: Planetary systems – Infrared: stars

---

*Send offprint requests to:* habing@strw.leidenuniv.nl (H. J. Habing)

\* Based on observations with ISO, an ESA project with instruments funded by ESA Member States (especially the PI countries: France, Germany, The Netherlands and the United Kingdom) and with the participation of ISAS and NASA.

## 1. Introduction

In 1983, while using standard stars to calibrate the IRAS photometry, Aumann et al. (1984) discovered that Vega ( $\alpha$  Lyr), one of the best calibrated and most used photometric standards in the visual wavelength range, emits much more energy at mid- and far-infrared wavelengths than its photosphere produces. Because the star is not reddened Aumann et al. proposed that the excess IR radiation is emitted by small, interplanetary-dust particles in a disk rather than in a spherical envelope. This proposal was confirmed by Smith & Terrile (1984) who detected a flat source of scattered light around  $\beta$  Pic, one of the other Vega-like stars detected in the IRAS data (Gillett 1986), and the one with the strongest excess. The disk around Vega and other main-sequence stars is the remnant of a much stronger disk built up during the formation of the stars. Aumann et al. (1984) pointed out that such disks have a lifetime much shorter than the stellar age and therefore need to be rebuilt continuously; collisions between asteroids are a probable source of new dust (Weissman 1984). Except for the somewhat exceptional case of  $\beta$  Pic (Hobbs et al. 1985) and in spite of several deep searches no trace of any gas has ever been found in the disks around main-sequence stars; see e.g. Liseau (1999).

Since 1984 the search for and the study of remnant disks has made substantial progress by the discovery of numerous “fatter” disks around pre-main sequence stars that contain dust and gas; for overviews see Beckwith & Sargent (1996), Sargent & Welch (1993), van Dishoeck & Blake (1998). The IRAS data base also contains detections of Vega-like disks around red giant stars that have developed from A and F-type main-sequence stars (Plets et al. 1997).

The discovery of Aumann et al. has prompted deeper searches in the IRAS data base with different strategies (Aumann 1985; Walker & Wolstencroft 1988; Mannings

& Barlow 1998). For a review see Backman & Paresce (1993). Recently Plets & Vynckier (1999) have discussed these earlier results and concluded that a significant excess at  $60\mu\text{m}$  is found in  $13 \pm 10\%$  of all main sequence stars with spectral type A, F, G and K. Unfortunately all these studies based on IRAS data only were affected by severe selection effects and did not answer important questions such as: Will a star loose its disk when it grows older? On what time-scale? Does the presence of planets depend on the stellar main-sequence mass? Do multiple stars have disks more, or less frequently? Do stars that formed in clusters have disks less often? With such questions unanswered we clearly do not understand the systematics of the formation of solar systems.

Here we present results of a continuation with ISO (Kessler et al. 1996) of the successful search of IRAS. Our aim has been to obtain a better defined sample of stars. The major step forward in this paper is not in the detection of more remnant disks, but in reliable information about the presence *or absence* of a disk. Earlier reports on results from our program have been given in Habing et al. (1996), Dominik et al. (1998), Jourdain de Muizon et al. (1999) and Habing et al. (1999).

## 2. Selecting and preparing the sample

Stars were selected so that their photospheric flux was within our sensitivity limit. Any excess would then appear immediately. We also wanted to make certain that any excess flux should be attributed to a circumstellar disk and not to some other property of the star, such as circumstellar matter ejected during the stellar evolution or to the presence of a red companion.

In selecting our stars we used the following criteria:

- We selected main-sequence stars with an expected photospheric flux at  $60\mu\text{m}$  larger than 30 mJy. We started from a list of infrared flux densities calculated by Johnson & Wright (1983) for 2000 stars contained in a catalogue of stars within 25 pc by Woolley et al. (1970). The limit of 30 mJy was based on the sensitivity of ISOPHOT (Lemke et al. 1996) as announced before launch by Klaas et al. (1994).
- We removed all stars with peculiarities in their spectra for which an accurate infrared flux density could not be predicted. This made us eliminate all O and B stars (emission lines, free-free IR excess) and all M stars (molecular spectra not well understood).
- We also removed all spectroscopic double stars. Visual double stars were rejected when the companion lies within 1 arcminute *and* its  $V$ -magnitude differs by less than 5 magnitudes; any remaining companion will contribute less than 10% of the  $60\mu\text{m}$  flux as one may show through Eq. 1.
- We also excluded variable stars; the variability of all stars has been checked *a posteriori* using the photom-

etry in the band at  $0.6\mu\text{m}$  given in the Hipparcos catalogue (Perryman et al. 1997); in all cases the stellar magnitude is constant within 0.07 magnitude.

To illustrate what stars are bright enough to be included we use an equation that gives the stellar colour,  $(V - [60\mu\text{m}])$ , as a function of  $(B - V)$ . The equation has been derived empirically from IRAS data by Waters et al. (1987); we use a slightly different version given by H. Plets (private communication):

$$\begin{aligned} V - [60\mu\text{m}] = & 0.01 + 2.99(B - V) \\ & - 1.06(B - V)^2 + 0.47(B - V)^3 \end{aligned} \quad (1)$$

The zero point in this equation has a formal error of 0.01. Intrinsic, reddening-free  $(B - V)$  values must be used, but all our stars are nearby and we assume that the measured values are reddening-free. *A posteriori* we checked that we may safely ignore the reddening produced by the disks that we detected; only in the case of  $\beta$  Pic is a small effect expected. Adopting a flux density of 1.19 Jy for  $[60\mu\text{m}] = 0$  we find apparent-magnitude limits and distance limits of suitable main-sequence stars as summarized in Table 1. The distance limit varies strongly with spectral type.

**Table 1.** Apparent magnitude and distance from the Sun (in parsec) of main-sequence stars with a  $60\mu\text{m}$  flux density of 30 mJy.

Sp.Type	A0	A5	F0	F5	G0	G5	K0	K5
$V(\text{mag})$	4.0	4.4	4.8	5.2	5.7	6.0	6.8	7.4
$d(\text{pc})$	45	31	25	19	15	13	10	7.5

Table 2 contains basic data on all stars from the sample for which we present ISO data. Columns 1 and 2 contain the number of the star in the HD and in the Hipparcos Catalogue (Perryman et al. 1997) and column 3 the name.  $V$  and  $B - V$  have been taken from the Geneva photometric catalogue (Kunzli et al. 1997). Columns 6 and 7 contain the distance and the spectral type as given in the Hipparcos Catalog (Perryman et al. 1997). The age given in column 8 is from Lachaume et al. (1999), where errors in the age determinations are discussed. The effective temperature in column 11 has been derived by fitting Kurucz' model atmospheres to the Geneva photometry; we will need this temperature to calculate the dust mass from the flux-density excess at  $60\mu\text{m}$ .

## 3. Measurements, data reduction, checks

### 3.1. Measurements

Pre-launch recommendations made us start with chopped measurements (observing mode PHT03; see Laureijs et al. (2000)) at  $60$ ,  $90$ ,  $135$  and  $170\mu\text{m}$ . After a few months of

**Table 2.** The stars of the sample

HD (1)	HIP (2)	Name (3)	V mag (4)	B-V mag (5)	d pc (6)	Spect. (7)	age Gyrs (8)	$T_{\text{eff}}$ K (9)
693	910	6 Cet	4.89	0.49	18.9	F5V	5.13	6210
1581	1599	$\zeta$ Tuc	4.23	0.58	8.6	F9V	6.46	5990
2151	2021	$\beta$ Hyi	2.82	0.62	7.5	G2IV	5.37	5850
4628	3765		5.74	0.89	7.5	K2V	7.94	5050
4813	3909	$\phi^2$ Cet	5.17	0.51	15.5	F7IV-V	1.38	6250
7570	5862	$\nu$ Phe	4.97	0.57	15.1	F8V	3.16	6080
9826	7513	50 And	4.10	0.54	13.5	F8V	2.88	6210
10700	8102	$\tau$ Cet	3.49	0.73	3.6	G8V	7.24	5480
10780	8362		5.63	0.80	10.0	K0V	2.82	5420
12311	9236	$\alpha$ Hyi	2.86	0.29	21.9	F0V	0.81	7080
13445	10138		6.12	0.81	10.9	K0V	5.37	5400
14412	10798		6.33	0.72	12.7	G8V	7.24	5420
14802	11072	$\kappa$ For	5.19	0.61	21.9	G2V	5.37	5850
15008	11001	$\delta$ Hyi	4.08	0.03	41.5	A3V	0.45	8920
17051	12653	$\iota$ Hor	5.40	0.56	17.2	G3IV	3.09	6080
17925	13402		6.05	0.86	10.4	K1V	0.08	5000
19373	14632	$\iota$ Per	4.05	0.60	10.5	G0V	3.39	6040
20630	15457	$\kappa^1$ Cet	4.84	0.68	9.2	G5Vv	0.30	5750
20766	15330	$\zeta^1$ Ret	5.53	0.64	12.1	G2V	4.79	5750
20807	15371	$\zeta^2$ Ret	5.24	0.60	12.1	G1V	7.24	5890
22001	16245	$\kappa$ Ret	4.71	0.41	21.4	F5IV-V	2.04	6620
22049	16537	$\epsilon$ Eri	3.72	0.88	3.2	K2V	0.33	5000
22484	16852	10 Tau	4.29	0.58	13.7	F9V	5.25	5980
23249	17378	$\delta$ Eri	3.52	0.92	9.0	K2V	7.59	5000
26965	19849	$\sigma^2$ Eri	4.43	0.82	5.0	K1V	7.24	5100
30495	22263	58 Eri	5.49	0.63	13.3	G3V	0.21	5820
33262	23693	$\zeta$ Dor	4.71	0.53	11.7	F7V	2.95	6160
34411	24813	$\lambda$ Aur	4.69	0.63	12.7	G0V	6.76	5890
37394	26779		6.21	0.84	12.2	K1V	0.34	5100
38392			6.15	0.94	9.0	K2V	0.87	4950
38393	27072	$\gamma$ Lep	3.59	0.48	9.0	F7V	1.66	6400
38678	27288	$\zeta$ Lep	3.55	0.10	21.5	A2Vann	0.37	8550
39060	27321	$\beta$ Pic	3.85	0.17	19.3	A3V	0.28	8040
43834	29271	$\alpha$ Men	5.08	0.71	10.2	G5V	7.24	5630
48915	32349	$\alpha$ CMa	-1.44	0.01	2.6	A0m		9920
50281	32984		6.58	1.07	8.7	K3V	2.63	5000
61421	37279	$\alpha$ CMi	0.40	0.43	3.5	F5IV-V	1.70	6700
74956	42913	$\delta$ Vel	1.93	0.04	25.0	A1V	0.35	9200
75732	43587	$\rho^1$ Cnc	5.96	0.87	12.5	G8V	5.01	5300
80007	45238	$\beta$ Car	1.67	0.07	34.1	A2IV		8600
95418	53910	$\beta$ UMa	2.34	0.03	24.4	A1V	0.36	9530
102647	57632	$\beta$ Leo	2.14	0.09	11.1	A3Vvar	0.24	8580
102870	57757	$\beta$ Vir	3.59	0.52	10.9	F8V	2.63	6180
103287	58001	$\gamma$ UMa	2.41	0.04	25.7	A0V SB	0.38	9440
106591	59774	$\delta$ UMa	3.32	0.08	25.0	A3Vvar	0.48	8630
110833	62145		7.01	0.94	15.1	K3V	12.60	5000
112185	62956	$\epsilon$ UMa	1.76	-0.02	24.8	A0p	0.30	9780
114710	64394	$\beta$ Com	4.23	0.57	9.2	G0V	3.63	6030
116842	65477	80 UMa	3.99	0.17	24.9	A5V	0.32	8000
126660	70497	$\theta$ Boo	4.04	0.50	14.6	F7V	2.95	6280
128167	71284	$\sigma$ Boo	4.46	0.36	15.5	F3Vwvar	1.70	6770
134083	73996	45 Boo	4.93	0.43	19.7	F5V	1.82	6500
139664	76829	$g$ Lup	4.64	0.41	17.5	F5IV-V	1.12	6680
142373	77760	$\chi$ Her	4.60	0.56	15.9	F9V	8.51	5840
142860	78072	$\gamma$ Ser	3.85	0.48	11.1	F6V	3.24	6330
149661	81300	12 Oph	5.77	0.83	9.8	K2V	2.09	5200
154088	83541		6.59	0.81	18.1	K1V	7.24	5000
156026	84478		6.33	1.14	6.0	K5V	0.63	4350
157214	84862	72 Her	5.38	0.62	14.4	G0V	7.24	5790
157881	85295		7.54	1.36	7.7	K7V	5.25	3950
160691	86796	$\mu$ Ara	5.12	0.69	15.3	G5V	6.17	5750
161797	86974	$\mu$ Her	3.42	0.75	8.4	G5IV	4.79	5670
166620	88972		6.38	0.88	11.1	K2V	7.24	4970
172167	91262	$\alpha$ Lyr	0.03	0.00	7.8	A0Vvar	0.35	9620
173667	92043	110 Her	4.19	0.48	19.1	F6V	2.40	6370
185144	96100	$\sigma$ Dra	4.67	0.79	5.8	K0V	5.50	5330
185395	96441	$\theta$ Cyg	4.49	0.40	18.6	F4V	1.29	6750
187642	97649	$\alpha$ Aql	0.76	0.22	5.1	A7IV-V	1.23	7550
188512	98036	$\beta$ Aql	3.71	0.86	13.7	G8IV	4.27	5500
190248	99240	$\delta$ Pav	3.55	0.75	6.1	G5IV-Vvar	5.25	5650
191408	99461		5.32	0.87	6.0	K2V	7.24	4700
192310	99825		5.73	0.88	8.8	K3V		5000
197692	102485	$\psi$ Cap	4.13	0.43	14.7	F5V	2.00	6540
198149	102422	$\eta$ Cep	3.41	0.91	14.3	K0IV	7.94	5000
203280	105199	$\alpha$ Cep	2.45	0.26	15.0	A7IV-V	0.89	7570
203608	105858	$\gamma$ Pav	4.21	0.49	9.2	F6V	10.50	6150
207129	107649		5.57	0.60	15.6	G2V	6.03	5930
209100	108870	$\zeta$ Ind	4.69	1.06	3.6	K5V	1.29	4600
215789	112623	$\epsilon$ Gru	3.49	0.08	39.8	A3V	0.54	8420
216956	113368	$\alpha$ Psa	1.17	0.15	7.7	A3V	0.22	8680
217014	113357	51 Peg	5.45	0.67	15.4	G5V	5.13	5810
219134	114622		5.57	1.00	6.5	K3Vvar	12.60	4800

operation of the satellite it appeared that at 60 and 90  $\mu\text{m}$  the on-off signal was strongly distorted by transients in the responsitivity of the detectors. Similarly, chopping appeared to be an inadequate observing mode at 135 and at 170  $\mu\text{m}$  because of confusion with structure in the background from infrared cirrus. We therefore switched to the observing mode PHT22 and made minimaps. Minimaps consumed more observing time and we therefore dropped the observations at 90 and 135  $\mu\text{m}$ . We tried to reobserve in minimap mode those targets that had already been observed in chopped mode (using extra time allocated when ISO lived longer than expected) but succeeded only partially: several targets had left the observing window. In total we used 65 hrs of observations. In this article we discuss only the stellar flux densities derived from the 60 and 170  $\mu\text{m}$  minimaps. Appendix A contains a detailed description of our measurement procedure.

Instrumental problems (mainly detector memory effects) made us postpone the reduction of the chopped measurements until a later date; this applies also to the many (all chopped) measurements at 25  $\mu\text{m}$ .

We added published (Ábrahám et al. 1998) ISOPHOT measurements of five A-type stars ( $\beta$  UMa,  $\gamma$  UMa,  $\delta$  UMa,  $\epsilon$  UMa and 80 UMa). The measurements have been obtained in a different mode from our observations, but we treat all measurements equally. These five stars are all at about 25 pc (Perryman et al. 1997), sufficiently nearby to allow detection of the photospheric flux. These stars are spectroscopic doubles and they do not fulfill all of our selection criteria; below we argue why we included them anyhow. Ábrahám et al. (1998) present ISOPHOT measurements of four more stars, which they assume to be at the same distance because all nine stars are supposed to be members of an equidistant group called the “Ursa Major stream”. The Hipparcos measurements (Perryman et al. 1997), however, show that four of the nine stars are at a distance of 66 pc and thus too far away to be useful for our purposes.

### 3.2. Data reduction

All our data have been reduced using standard calibration tables and the processing steps of OLP6/PIA7. These steps include the instrumental corrections and photometric calibration of the data. At the time when we reduced our data there did not yet exist a standard procedure to extract the flux. We therefore developed and used our own method- see appendix B.

Later versions of the software which contain upgrades of the photometric calibration do not significantly alter our photometric results and the conclusions of this paper remain unchanged. For each filter the observing mode gave two internal calibration measurements which were closely tuned to the actual sky brightness. This makes the absolute calibration insensitive to instrumental effects as filter-to-filter calibrations and signal non-linearities which

were among others the main photometric calibration improvements for the upgrades. In addition, it is standard procedure to ensure that each upgrade does not degrade the photometric calibration of the validated modes of the previous processing version.

## 4. Results

### 4.1. Flux densities at 60 $\mu\text{m}$

The flux densities at 60  $\mu\text{m}$  are presented in Table 3. The content of each column is as follows: (1): the HD number; (2): the TDT number as used in the ISO archive; (3) the flux density corrected for bandwidth effects (assuming that the spectrum is characterized by the Rayleigh-Jeans equation) and for the fact that the stellar flux extended over more than 1 pixel; (4) the error estimate assigned by the ISOPHOT software to the flux measurement in column (3); for the IRAS measurements the error has been put at 100 mJy; (5) the flux expected from the stellar photosphere,  $F_\nu^{\text{pred}}$  as derived from Eq. 1 using the  $V$  and  $(B - V)$  values in Table 2; (6): the difference between columns (3) and (5); we call it the “excess flux”,  $F_\nu^{\text{exc}}$ ; (7): the ratio of the excess flux compared to the measurement error given in column (4); when we concluded that the excess is real and not a measurement error we recalculated the monochromatic flux density by assuming a flat spectrum within the ISOPHOT 60  $\mu\text{m}$  bandwidth; the result is in column (8) and is called  $F_\nu^{\text{disk}}$ . Column (9) shows an estimate of  $\tau_{60}^{\text{disk}}$ , the optical depth of the disk at visual wavelengths, but estimated from the flux density at 60  $\mu\text{m}$ ; see below for a definition and see appendix D for more details. Flux densities in columns 3, 4, 6 and 7 have been corrected for the point spread function being larger than the pixel size of the detector and for Rayleigh-Jeans colour-correction (cc); for ISO fluxes, the inband flux has been divided by 0.69 (the correction for the point spread function (=psf), see Appendix B) and by 1.06 (cc) and for IRAS fluxes, the IFSC or IPSC flux have been divided by 1.31 (cc). The “disk emission” in column 8 is “de-colour-corrected” from column 6.

We have checked the quality of our results at 60  $\mu\text{m}$  in two ways: (i) by comparing ISO with IRAS flux densities; (ii) by comparing fluxes measured by ISO with predictions based on the  $(B - V)$  photometric index. The second approach allows us to assess the quality of ISO flux densities below the IRAS sensitivity limit.

### 4.2. The correlation between IRAS and ISO measurements at 60 $\mu\text{m}$

Fig. 1 shows the strong correlation between IRAS and ISO 60  $\mu\text{m}$  flux densities down to about the 60 mJy level of ISO. For three of the fainter stars the IRAS fluxes are considerably higher than those of ISO. For one of these three, HD 142860, the ISO measurements show the presence of two nearby 60  $\mu\text{m}$  sources; the larger IRAS beam

**Table 3.** 60  $\mu$ m data: see text for an explanation of the various columns

HD	ISO_id	$F_\nu$ mJy	$\sigma_\nu$ mJy	$F_\nu^{\text{pred}}$ mJy	$F_\nu^{\text{exc}}$ mJy	$F_\nu^{\text{exc}}/\sigma_\nu$	$F_\nu^{\text{disk}}$ mJy	$\log \tau_{60}^{\text{disk}}$	Reference
(1)	(2)	(3)	(4)	(5)	(6)	(7)	(8)	(9)	(10)
693	74900501	33	34	43	-10	< 1		< -4.6	ISO minimap
1581	69700102	94	19	94	0	< 1		< -5.0	ISO minimap
2151		351	100	376	-25	< 1			IFSC
4628	61901104	41	24	44	-4	< 1		< -4.1	ISO minimap
4813	61901705	55	37	34	20	< 1		< -4.3	ISO minimap
7570	72002506	85	25	47	38	1.6		< -4.4	ISO minimap
9826	61503786	100	22	98	2	< 1		< -5.0	ISO minimap
10700	75701121	433	37	253	180	4.9	190	-4.6	ISO minimap
10780	61503507	43	30	41	3	< 1		< -4.1	ISO minimap
12311	69100108	189	18	178	10	< 1		< -5.6	ISO minimap
13445	73100771	25	24	26	-2	< 1		< -4.1	ISO minimap
14412	76301673	-12	14	18	-30	< 1		< -4.4	ISO minimap
14802	80201174	56	19	41	14	< 1		< -4.5	ISO minimap
15008	71801511	41	9	30	10	1.1		< -5.4	ISO minimap
17051	76500413	45	15	31	14	< 1		< -4.5	ISO minimap
17925	78100314	104	24	31	73	3.1	80	-3.9	ISO minimap
19373	81001847	122	13	116	6	< 1		< -5.2	ISO minimap
20630	79201553	9	33	66	-57	< 1		< -4.9	ISO minimap
20766	69100715	34	24	32	2	< 1		< -4.4	ISO minimap
20807	57801756	30	13	39	-9	< 1		< -4.9	ISO minimap
22001	69100659	52	9	42	9	1.0		< -5.1	ISO minimap
22049		1250	100	278	967	9.7	1260		IFSC
22484	79501562	141	27	89	51	1.9		< -4.6	ISO minimap
23249		270	100	363	-92	< 1			IFSC
26965	84801865	121	21	128	-7	< 1		< -4.7	ISO minimap
30495	83901668	174	31	33	141	4.5	150	-4.1	ISO minimap
33262	58900871	81	21	55	26	1.3		< -4.7	ISO minimap
34411	83801474	63	13	69	-5	< 1		< -5.0	ISO minimap
37394	83801977	40	13	26	14	1.0		< -4.0	ISO minimap
38392	70201402	31	24	34	-2	< 1		< -3.9	ISO minimap
38393	70201305	160	25	138	22	< 1		< -5.1	ISO minimap
38678	69202308	349	22	60	289	13.3	310	-4.7	ISO minimap
39060	70201080	14700	346	54	14650	42.4	15500	-2.8	ISO minimap
43834	62003217	48	16	56	-8	< 1		< -4.8	ISO minimap
48915	72301711	4230	155	4650	-420	< 1		< -7.5	ISO minimap
50281	71802114	-4	16	30	-33	< 1		< -4.3	ISO minimap
61421		2290	100	2350	-59	< 1		< -6.0	IFSC
74956		399	100	226	173	1.7			IPSC
75732	17800102	160	28	35	126	4.4	130	-3.8	Dominik et al. 1998
80007		284	100	311	-27	< 1			IFSC
95418	19700563	539	135	152	387	2.9	410	-5.0	Ábrahám et al. 1998
102647		784	100	213	571	5.7	750	-4.8	IFSC
102870		137	100	150	-14	< 1		< -4.6	IFSC
103287	19500468	164	41	147	17	< 1		< -5.5	Ábrahám et al. 1998
106591	19700973	94	59	69	25	< 1		< -4.9	Ábrahám et al. 1998
110833	60000526	-7	14	15	-22	< 1			ISO minimap
112185	34600578	322	81	223	99	1.2		< -5.4	Ábrahám et al. 1998
114710	61000119	106	34	93	13	< 1		< -4.7	ISO minimap
116842	19500983	40	34	47	-7	< 1			Ábrahám et al. 1998
126660	61000834	93	21	95	-2	< 1		< -5.1	ISO minimap
128167	61001236	100	19	48	52	2.8	55	-5.0	ISO minimap
134083	61001337	70	26	36	34	1.3		< -4.5	ISO minimap
139664	64700880	488	48	45	442	9.2	470	-4.0	ISO minimap
142373	61001139	71	21	64	6	< 1		< -4.8	ISO minimap
142860	63102981	113	24	109	4	< 1		< -5.1	ISO minimap
149661	80700365	56	22	38	18	< 1		< -4.1	ISO minimap
154088	64702041	40	55	17	22	< 1		< -3.3	ISO minimap
156026	64702142	30	34	43	-13	< 1		< -3.4	ISO minimap
157214	71000144	27	26	36	-8	< 1		< -4.4	ISO minimap
157881	65000845	41	22	24	17	< 1		< -2.6	ISO minimap
160691	64402347	73	18	52	21	1.2		< -4.5	ISO minimap
161797		222	100	281	-59	< 1		< -4.6	IFSC
166620	71500648	41	21	24	17	< 1		< -3.8	ISO minimap
172167	71500582	6530	217	1170	5360	24.7	5700	-4.8	ISO minimap
173667	71500883	78	12	80	-1	< 1		< -5.3	ISO minimap
185144	69500449	92	21	96	-5	< 1		< -4.7	ISO minimap
185395	69301251	63	34	51	12	< 1		< -4.7	ISO minimap
187642	72400584	1010	66	1050	-41	< 1		< -6.1	ISO minimap
188512		257	100	269	-12	< 1			IFSC
190248		174	100	250	-76	< 1		< -4.6	IFSC
191408	72501252	43	37	62	-19	< 1		< -4.0	ISO minimap
192310	70603454	73	13	44	29	2.2		< -4.1	ISO minimap
197692	70603356	68	18	76	-8	< 1		< -5.2	ISO minimap
198149		552	100	393	159	1.6			IFSC
203280	61002158	253	49	243	10	< 1		< -5.4	ISO minimap
203608	72300260	109	21	80	30	1.4		< -4.9	ISO minimap
207129	13500820	275	55	29	246	4.5	260	-3.8	Jourdain de Muizon et al. 1999
209100	70800865	146	24	166	-19	< 1		< -4.4	ISO minimap
215789	71801167	74	16	60	14	< 1		< -5.4	ISO minimap
216956	71800269	6930	204	605	6320	31.0	6700	-4.3	ISO minimap
217014	73601191	1	24	37	-36	< 1		< -4.7	ISO minimap
219134	75100962	17	15	65	-48	< 1			ISO minimap

**Table 4.** Flux densities measured at 170  $\mu$ m. The various columns have the same meaning as in the previous table

HD	ISO_id	$F_\nu$ mJy	$\sigma_\nu$ mJy	$F_\nu^{\text{pred}}$ mJy	$F_\nu^{\text{exc}}$ mJy	$F_\nu^{\text{exc}}/\sigma_\nu$	$F_\nu^{\text{disk}}$ mJy	$\log \tau_{170}^{\text{disk}}$
(1)	(2)	(3)	(4)	(5)	(6)	(7)	(8)	(9)
693	37500903	12	13	5	7	< 1		
4628	39502509	-10	9	5	-15	< 1		
4813	38701512	12	10	4	8	< 1		
7570	38603615	14	36	5	9	< 1		
9826	42301521	-22	82	10	-32	< 1		
10700	39301218	125	21	28	97	4.7	120	-5.4
10780	45701321	180	626	4	176	< 1		
12311	69100209	98	52	19	79	1.5		
14412	40101733	-20	12	2	-22	< 1		
14802	40301536	1	16	5	-4	< 1		
15008	75000612	23	49	3	20	< 1		
17051	41102842	4	9	3	1	< 1		
19373	81001848	-163	182	11	-174	< 1		
20630	79201554	-122	85	6	-128	< 1		
20807	57801757	73	17	4	69	4.1	80	-4.8
22001	69100660	-49	25	5	-54	< 1		
22484	79501563	7	21	9	-2	< 1		
26965	84801866	60	38	16	44	1.2		
30495	83901669	51	25	4	47	1.9		
33262	58900872	-33	33	6	-39	< 1		
34411	83801475	-59	98	7	-66	< 1		
37394	83801978	61	57	3	58	1.0		
38392	70201403	25	20	4	21	1.1		
38393	70201306	68	8	14	54	6.9	65	-5.4
38678	69202309	22	48	6	16	< 1		
39060	70201081	3807	143	6	3801	26.5	4600	-3.2
48915	72301712	184	401	456	-272	< 1		
50281	71802115	-826	268	2	-828	< 1		
95418	19700564	133	73	13	120	1.6		
103287	19500469	95	117	12	83	< 1		
106591	33700130	-5	17	7	-12	< 1		
110833	60000527	-31	23		-31	< 1		
112185	34600579	-35	65	21	-56	< 1		
126660	61000935	-39	20	10	-49	< 1		
128167	39400840	56	12	6	50	4.3	60	-5.0
139664	29101241	122	207	5	117	< 1		
142373	62600340	-12	31	8	-20	< 1		
142860	30300242	31	73	12	19	< 1		
149661	30400943	113	69	4	109	1.6		
154088	45801569	-138	137	2	-140	< 1		
156026	83400343	-383	318	6	-389	< 1		
157214	33600844	-31	34	4	-35	< 1		
160691	29101345	-171	65	5	-176	< 1		
166620	36901487	-9	21	3	-12	< 1		
172167	44300846	2621	142	123	2498	17.6	3000	-4.8
173667	31902147	-53	91	8	-61	< 1		
185395	35102048	-35	26	5	-40	< 1		
197692	70603857	27	34	8	19	< 1		
203608	72300361	-52	9	10	-62	< 1		
207129	34402149	293	23	3	290	12.4	350	-4.0
217014	37401642	-57	23	4	-61	< 1		
222368	37800836	-30	59	10	-40	< 1		

*Note:* Fluxes in columns 3,4,6,7 are corrected for point spread function and Rayleigh-Jeans colour-correction, i.e. the inband flux has been divided by 0.64 (psf) and by 1.2 (cc). The “Excess” in column 8 is “de-colour-corrected” from column 6.

has merged the three sources; see Fig. 4. For the two remaining sources in Fig. 1 with different IRAS and ISO flux densities we assume that the IRAS measurement is too high because noise lifted the measured flux density above the detection limit, a well-known effect for measurements close to the sensitivity limit of a telescope.

#### 4.3. The correlation between predicted and measured flux densities at 60 $\mu$ m

A strong correlation exists between predicted and measured flux density, columns (8) and (3) in Table 3, as seen in Fig. 2.

Fig. 3 shows that the distribution of the excess fluxes can be split into two components: a very narrow distribution around zero plus a strong wing of positive excesses, i.e. cases where we measure more flux than is produced by the stellar photosphere. In these cases a disk is very probably present. A Gauss curve has been drawn in the figure with parameters  $\mu = 4$  mJy and  $\sigma = 21$  mJy, where  $\mu$  is the average and  $\sigma$  the dispersion. The value of  $\sigma$  agrees with the magnitude of individual error measurements as given in column 8 in Table 3. The one case in Fig. 3 with a strong negative excess, i.e. where we measured less than is predicted, concerns Sirius,  $\alpha$  CMa; we interpret this negative excess as a consequence of the poor correction for

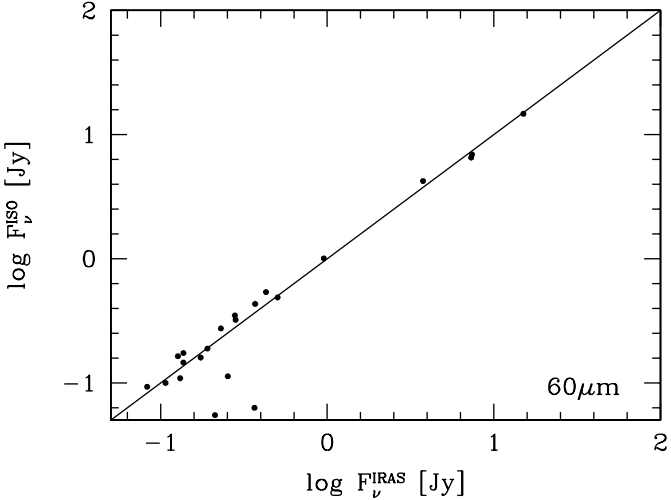


**Fig. 1.** Correlation of fluxes measured by IRAS and by ISO, respectively. The line marks the relation  $F_\nu^{\text{IRAS}} = F_\nu^{\text{ISO}}$ .

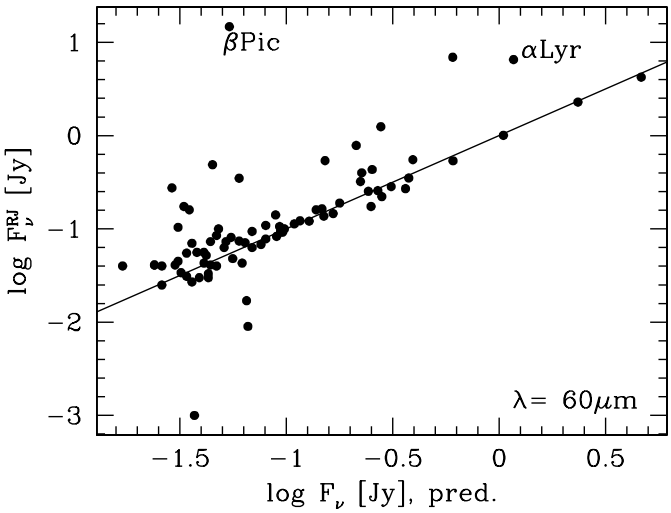


**Fig. 2.** Diagram of predicted and measured fluxes at  $60 \mu\text{m}$ . The predicted fluxes were derived mainly from Eq. (1) except in a few cases where Kurucz model atmospheres were fitted to photometric points at optical wavelengths. See text. The line marks the relation  $F_\nu = F_\nu^{\text{pred}}$ .

transient effects of the detector for this strong infrared source.

We have concluded that a disk is present when  $F_\nu^{\text{exc}} > \mu + 3\sigma = 65 \text{ mJy}$ . A summary of data on all stars with disks is in Table 6. HD 128167 has also been labelled as a “detection” although  $F_\nu^{\text{exc}}$  is only  $2.8\sigma_\nu$ . The star is one of the few with a detection at  $170 \mu\text{m}$  and this removed our doubts about the detection at  $60 \mu\text{m}$ .

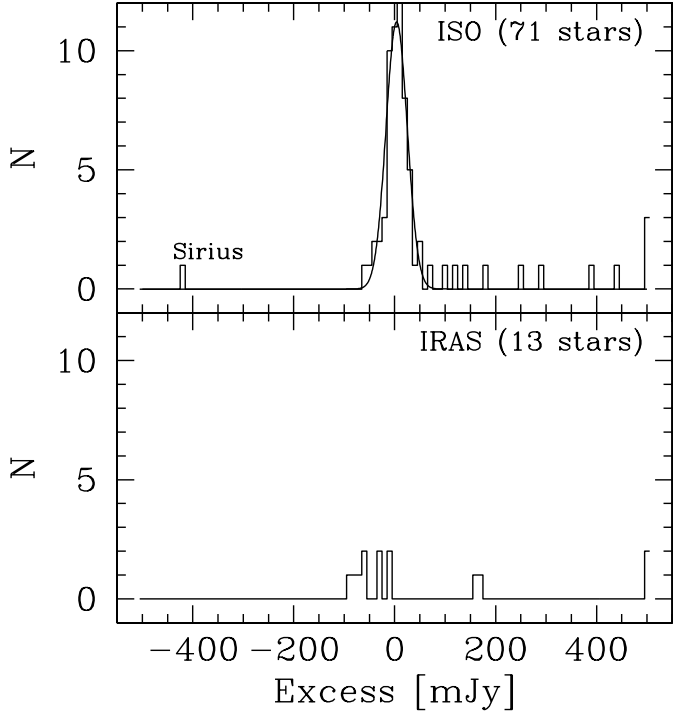


**Fig. 3.** Histogram of the differences between the measured flux density and the one predicted at  $60 \mu\text{m}$ . Top: distribution of the flux densities measured by ISO; there are three stars with an excess higher than  $500 \text{ mJy}$ ; the drawn curve is a Gauss curve with average  $\mu = 4 \text{ mJy}$  and dispersion  $\sigma = 21 \text{ mJy}$ . Bottom: the same for stars where only IRAS data are available; two stars have an excess higher than  $500 \text{ mJy}$ .

#### 4.4. Results at $170 \mu\text{m}$

The results are shown in Table 4 which has the same structure as Table 3. IRAS did not measure beyond  $100 \mu\text{m}$  and we have no existing data to compare with our ISO data. Neither can we make a useful comparison between measured and predicted flux densities because the photospheric flux is expected to be roughly  $1/8$  of the  $60 \mu\text{m}$  flux density and for most stars this is below the sensitivity limit of ISO.

We accepted fluxes as real when  $F_\nu^{\text{exc}} > 3\sigma_\nu$  and the minimap showed flux only in the pixel illuminated by the star. This leads to seven detections at  $170 \mu\text{m}$  in Table 4. All seven stars have excess emission also at  $60 \mu\text{m}$  except HD 20807 and HD 38393. Very probably these last two stars have accidentally been misidentified with unrelated background sources, as we will show now.

#### 4.5. Should some detections be identified with unrelated field sources?

We need to consider the possible influence of the field-source population upon our results.

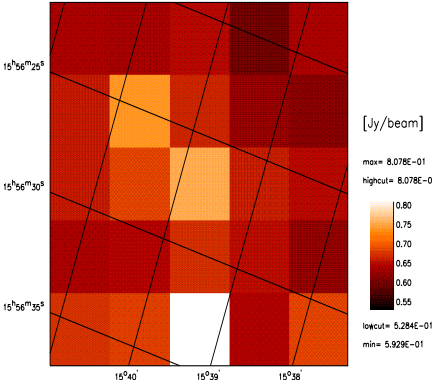


**Fig. 4.** The  $60\text{ }\mu\text{m}$  image in spacecraft orientation of the region around HD 142860 as obtained from the ISOPHOT minimap. There are three point sources in the field, the position of the source in the centre corresponds to the position of HD142860. The upper source has  $F_\nu = 140 \pm 40$  mJy and coordinates (J2000) RA  $15^{\text{h}}56^{\text{m}}25^{\text{s}}$ , Dec  $15^{\circ}40'43''$ ; the lower source has  $F_\nu = 250 \pm 40$  mJy and coordinates (J2000) RA  $15^{\text{h}}56^{\text{m}}33^{\text{s}}$ , Dec.  $15^{\circ}39'15''$ .

Dole et al. (2000), Matsuhara et al. (2000), Oliver et al. (2000) and Elbaz et al. (2000) quote source counts at respectively  $170$ ,  $90$  and  $15\text{ }\mu\text{m}$  from which the surface density of sources on the sky can be read down to the sensitivity limits of our measurements. In the  $170$  and  $90\text{ }\mu\text{m}$  cases this involves the authors' extrapolations, via models, of their source counts from the roughly  $100\text{--}200$  mJy flux limits of their respective datasets. At  $60\text{ }\mu\text{m}$  source counts can be approximated, with sufficient accuracy for present purposes, by interpolation from the other wavelengths. Using these source densities we now estimate the probability that our samples of detections contain one or two field sources unrelated to the star in question.

Since we know, for all of our targets, into exactly which pixel of the PHT map they should fall, we need to consider the probability that a field source with flux down to our sensitivity limit falls into the relevant PHT pixel. This effective “beam” area is  $45'' \times 45''$  and  $100'' \times 100''$ , at  $60$  and  $170\text{ }\mu\text{m}$  respectively.

At  $60\text{ }\mu\text{m}$  we have explored 84 beams (targets) and at  $170\text{ }\mu\text{m}$  52 beams (targets). We apply the binomial distribution to determine the probability  $P(q, r)$  that at least  $r$  spurious detections occur in  $q$  trials when the probability per observation equals  $p$ .

Table 5 lists the following parameters: column(1) shows the wavelength that we consider; column (3) contains the probability  $p$  to find a source in any randomly chosen pixel with a flux density above the limit  $F_\nu^{\text{lim}}$  given in column (2). Column (4) lists the number  $q$  of targets (i.e. trials) in the  $60$  and  $170\text{ }\mu\text{m}$  samples. Columns (5)–(7) give the probability  $P(q, r)$  of finding at least 1, 2 and 3 spurious detections with  $F_\nu > F_\nu^{\text{lim}}$  within a sample of size  $q$ .

**Table 5.** Probability of spurious detections

$\lambda$ $\mu\text{m}$	$F_\nu^{\text{lim}}$ mJy	$p$	$q$	$P(q, 1)$	$P(q, 2)$	$P(q, 3)$
60	100	0.006	84	0.397	0.091	
60	150	0.0015	84	0.117	0.007	
60	200	0.001	84	0.079	0.003	
170	50	0.15	52	1.000	0.997	0.988
170	100	0.07	52	0.975	0.881	0.702
170	200	0.04	52	0.875	0.61	0.334
170	300	0.005	52	0.226	0.027	
170	1000	0.00025	52	0.013		

#### 4.5.1. Probability of spurious detections at $60\text{ }\mu\text{m}$

It follows from Table 5 that there is a 40% chance that at least one of the two detections at  $60\text{ }\mu\text{m}$  below 100 mJy is due to a field source, and there is a 9% chance that both are.

If we ignore field sources and consider the likelihood of spurious excesses occurring above a  $3\sigma$  detection-limit due purely to statistical fluctuations in the measurements, we find that random noise contributes (coincidentally) a further 0.006 spurious detections per beam, on average, for the faintest detections (near  $3\sigma$ ).

The cumulative probability, therefore, is 0.64 that at least 1 of the two detections at  $60\text{ }\mu\text{m}$  below 100 mJy is not related to a disk; the probability is 0.17 that they are both spurious.

#### 4.5.2. Probability of spurious detections at $170\text{ }\mu\text{m}$

Table 4 lists 3 detections below 100 mJy. Two (HD 20630 and 38393) have not been detected at  $60\text{ }\mu\text{m}$ . Table 5 shows that the probability is high that both are background sources unrelated to the two stars in question. In the further discussion these two stars have been considered to be without a disk. The third source with a  $170\text{ }\mu\text{m}$  flux density below 100 mJy, HD 128167, has been detected also at  $60\text{ }\mu\text{m}$ . We assume that this detection is genuine and that the source coincides with the star. The remaining four detections at  $170\text{ }\mu\text{m}$  with  $F_\nu > 100$  mJy are also correctly identified with the appropriate star.

## 5. Discussion

Data for the stars with a disk are summarized in Table 6. Each column contains quantities defined and used in earlier tables with the exception of the last column that contains an estimate of the mass of the disk,  $M_d$ .

### 5.1. Comparison with the IRAS heritage

The overall good agreement between the IRAS and ISO measurements has already been discussed. The IRAS data base has been explored by several different groups in

**Table 6.** The  $60\mu\text{m}$  excess stars

HD (1)	Name (2)	Spect. (3)	age Gyrs (4)	60 $\mu\text{m}$				170 $\mu\text{m}$				$M_d$ $10^{-5} M_{\oplus}$ (12)
				$F_{\nu}$ mJy (5)	$\sigma_{\nu}$ mJy (6)	$F_{\nu}^{\text{disk}}$ mJy (7)	$10 \log \tau_{60}^{\text{disk}}$ (8)	$F_{\nu}$ mJy (9)	$\sigma_{\nu}$ mJy (10)	$F_{\nu}^{\text{disk}}$ mJy (11)		
10700	$\tau$ Cet	G8V	7.24	433	37	190	-4.6	125	21	120	20	
17925		K1V	0.08	104	24	80	-3.9				108	
22049	$\epsilon$ Eri	K2V	0.33	1250	100	1260						
30495	58 Eri	G3V	0.21	174	31	150	-4.1	51	25		73	
38678	$\zeta$ Lep	A2Vann	0.37	349	22	310	-4.7	22	48		18	
39060	$\beta$ Pic	A3V	0.28	14700	346	15500	-2.8	3810	143	4600	1200	
75732	$\rho^1$ Cnc	G8V	5.01	160	28	130	-3.8				130	
95418	$\beta$ UMa	A1V	0.36	539	135	410	-5.0	133	290		8	
102647	$\beta$ Leo	A3V	0.24	784	100	750	-4.8				13	
128167	$\sigma$ Boo	F3Vwvar	1.70	100	19	55	-5.0	56	12	60	8	
139664	g Lup	F5IV-V	1.12	488	48	470	-4.0	122	830		84	
172167	$\alpha$ Lyr	A0Vvar	0.35	6530	217	5700	-4.8	2620	142	3000	13	
207129		G2V	6.03	275	55	260	-3.8	293	23	350	132	
216956	$\alpha$ PsA	A3V	0.22	6930	204	6700	-4.3				44	

Note: Fluxes in columns 5,6,9,10 are corrected for point spread function and Rayleigh-Jeans colour-correction. Excesses in columns 7 and 11 are “de-colour-corrected” from columns 5 and 9 respectively (see text).

search of more Vega-like stars. Backman & Paresce (1993) have reviewed most of these searches. Their table X contains all stars with disks. For nine of those in table X we have ISO measurements, and in eight cases these show the presence of a disk. The one exception is  $\delta$  Vel, HD 74956. We find excess emission but the excess is insignificant (only  $1.7\sigma$ ) and we did not include the star in table 6. Thus our data agree well with those discussed by Backman & Paresce (1993). Although ISO was more sensitive than IRAS at  $60\mu\text{m}$  by about a factor of 5 we have only one new detection of a disk: HD 17925, with an excess of 82 mJy at  $60\mu\text{m}$ .

Plets & Vynckier (1999) have analysed IRAS data in search of “Vega-like” stars and paid special attention to our list of candidate stars. In general there is good agreement between their conclusions and ours. Nine of the disk stars they find in IRAS we confirm with our ISO data. Four of the stars for which they find evidence of a disk at  $60\mu\text{m}$  are without excess emission in our sample. In two cases (HD 142860 and HD 215789) the difference IRAS/ISO is large: IRAS: 413 and 220 mJy; ISO: 113 and 78 mJy). In both cases we are of the opinion that at such low flux levels the ISO data are to be preferred over the IRAS data.

## 5.2. Differences with disks around pre-main-sequence stars

Disks have been found around many pre-main-sequence (=PMS) stars; here we discuss disks around main-sequence (=MS) stars. Disks around PMS stars are always detected by their molecular line emission; they contain dust and gas. The search for molecular emission lines in MS disks, however, has been fruitless so far (Liseau 1999). This is in line with model calculations by Kamp & Bertoldi (2000) who show that CO in disks around MS-stars will be dissociated by the interstellar radiation field. Recent ob-

servations with ISO indicate the presence of  $\text{H}_2$  in the disk around  $\beta$  Pic and HST spectra show the presence of CO absorption lines (van Dishoeck, private communication), but the disk around  $\beta$  Pic is probably much “fatter” than those around our MS-stars; it is not even certain that  $\beta$  Pic is a PMS or MS-star. We will henceforth assume that disks detected around MS-stars contain only dust and no gas.

## 5.3. A simple quantitative model

We have very little information on the disks: in most cases only the photometric flux at  $60\mu\text{m}$ . For the quantitative discussion of our measurements we will therefore use a very simple model. We assume a main-sequence star with an effective temperature  $T_{\text{eff}}$  and a luminosity  $L_{\star}$ . The star is surrounded by a disk of  $N$  dust particles. For simplicity, and to allow an easy comparison between different stars, we use a unique distance of the circumstellar dust of  $r = 50$  AU. This value is consistent with the measurements of spatially resolved disks like Vega and  $\epsilon$  Eri and also with the size of the Kuiper Belt in our own solar system. The particles are spherical, have all the same diameter and are made of the same material. The important parameter of the disk that varies from star to star is  $N$ . The temperature,  $T_d$ , of each dust particle is determined by the equilibrium between absorption of stellar photons and by emission of infrared photons; thus  $T_d$  depends on  $T_{\text{eff}}$ .

Each dust particle absorbs photons with an effective cross section equal to  $Q_{\nu} \pi a^2$ ;  $Q_{\nu}$  is the absorption efficiency of the dust and  $a$  the radius of a dust particle. The average of  $Q_{\nu}$  over the Planck function will be written as  $Q_{\text{ave}}$ . The dust particles absorb a fraction  $\tau \equiv N Q_{\text{ave}}(T_{\text{eff}}) a^2 / (4 r^2)$  of the stellar energy and reemit this amount of energy in the infrared; in all cases the value of  $\tau$  is very small. We will call  $\tau$  the “optical depth of the

disk"; it represents the extinction by the disk at visual wavelengths:

$$\tau = \frac{L_d}{L_*} = \frac{F_{\text{bol}}^d}{F_{\text{bol}}^{\text{pred}}}. \quad (2)$$

The mass of the disk,  $M_d$ , is proportional to  $\tau$ :

$$M_d = \frac{16\pi}{3} \frac{\rho a r^2}{Q_{\text{ave}}} \tau \quad (3)$$

We will use spheres with a radius  $a$  of  $1 \mu\text{m}$  and with material density  $\rho$  and optical constants of interstellar silicate (Draine & Lee 1984); we use  $Q_{\text{ave}} = 0.8$  and derive  $M_d = 0.5 \tau M_{\oplus}$ . It is known that the grains in Vega-like systems are much larger than interstellar grains. For A stars, the emission is probably dominated by grains larger than  $10 \mu\text{m}$  (Aumann et al. 1984; Zuckerman & Becklin 1993; Chini et al. 1991), because smaller grains are blown out by radiation pressure. However, for F, G, and K stars, the blowout sizes are  $1 \mu\text{m}$  or smaller and it must be assumed that the emission from these stars is dominated by smaller grains. We calculate mass estimates using the grain size of  $1 \mu\text{m}$ . Since the mass estimates depend linearly upon the grain size, the true masses of systems with bigger grains can easily be calculated by scaling the value. The mean absorption efficiency factor  $Q_{\text{ave}}$  is only weakly dependent upon the grain size for sizes between 1 and  $100 \mu\text{m}$ .

Numerical simulations made us discover a simple property of this model that is significant because it makes the detection probability constant for disks of stars of different spectral type. Define a variable called "contrast":  $C_{60} \equiv (L_{\nu,d}/L_{\nu,*})_{60 \mu\text{m}}$ , and assume black body radiation by the star and by the dust particles, then  $C_{60}$  is constant for  $T_{\text{eff}}$  in the range of A, F, and G-stars. The reason for this constancy is that when  $T_{\text{eff}}$  drops the grains get colder and emit less in total, but because  $60 \mu\text{m}$  is at the Wien side of the Planck curve, their emission rate at  $60 \mu\text{m}$  goes up. For a more elaborate discussion see appendix C. Let us then make a two-dimensional diagram of the values of  $\tau$  (or of  $M_d$ ) as a function of  $T_{\text{eff}}$  and  $C_{60}$ : see Fig. 5. Constant values of  $\tau$  appear as horizontal contours for  $T_{\text{eff}} > 5,000$  K. The triangles in the diagram represent the disks that we detected; small squares represent upper limits. The distribution of detections and upper limits makes clear that *we detected all disks with  $\tau > 2 \times 10^{-5}$  or  $M_d 1.0 \times 10^{-5} M_{\oplus}$  around the A, F, G-type stars in our sample of 84 stars*; we may, however, have missed a few disks around our K stars and we may have missed truncated and thus hot disks.

#### 5.4. The incidence and survival of remnant dust disks

The results discussed here have also been presented in Habing et al. (1999).

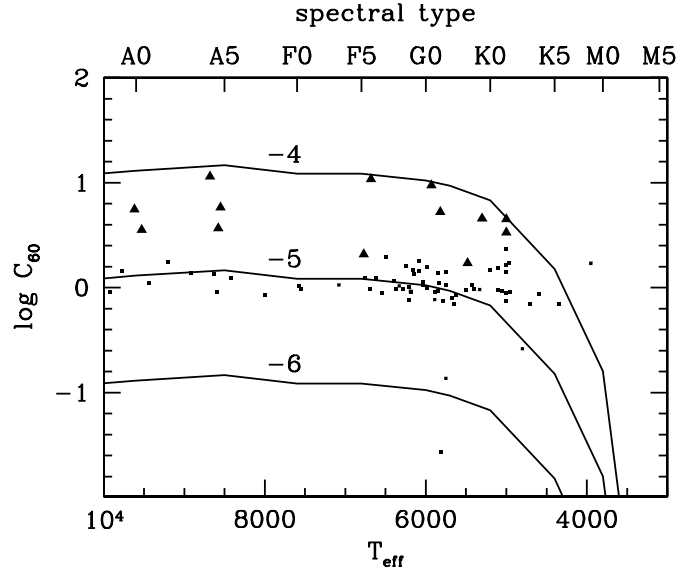


**Fig. 5.** The  $^{10}$ logarithm of the fraction of stellar energy emitted by the disk is shown as a function of  $T_{\text{eff}}$  and  $C_{60}$ . The labels to the curves indicate the  $^{10}$ logarithm of  $\tau$ . The triangles represent stars with a disk, and the small squares indicate the upper limit of non-detections. Using our standard dust particle model the mass of each disk is given by  $M_d = 0.5 \tau M_{\oplus}$  (see text).

Stellar ages have been derived in an accompanying paper (Lachaume et al. 1999). Errors in the determination of the ages have been given in that paper; occasionally they may be as large as a factor of 2 to 3; errors that large will not detract from our main conclusions.

#### 5.4.1. The question of completeness and statistical bias

Our sample has been selected from the catalogue of stars within 25 pc from the Sun by Woolley et al. (1970); this catalogue is definitely incomplete and so must be our sample. Even within the distance limits given in Table 1 stars will exist that we could have included but did not. This incompleteness does not, however, introduce a statistical bias: we have checked that for a given spectral type the distribution of the stellar distances is the same for stars with a disk as for stars without a disk; this is illustrated by the average distances in Table 7.

**Table 7.** : Average distances of stars with and without a disk

	# without disk (pc)	# with disk (pc)
A**	9 $22.6 \pm 11.0$	6 $16.8 \pm 7.1$
F**	21 $14.6 \pm 4.6$	2 $14.0 \pm \dots$
G**	17 $12.3 \pm 3.9$	4 $11.3 \pm 5.3$
K**	20 $9.5 \pm 3.8$	2 $6.6 \pm \dots$

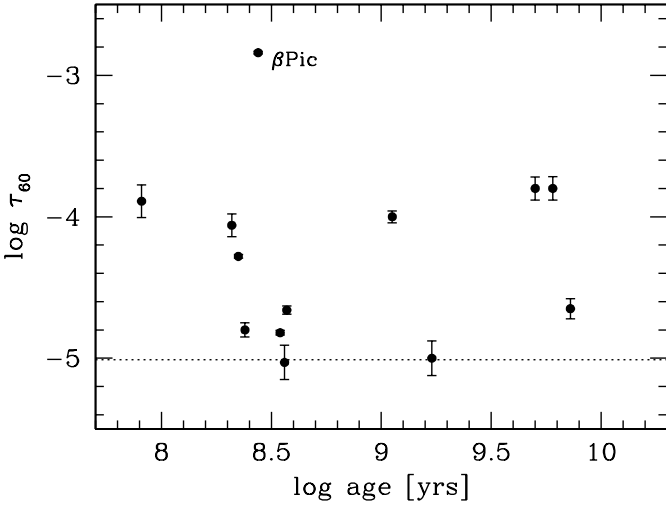


**Fig. 6.**  $\tau$ , the fraction of the stellar light reemitted at infrared wavelengths, is shown as a function of stellar age

#### 5.4.2. Detection statistics and stellar age

**Table 8.** : Detection statistics

	< 400 Myr		400-1000 Myr		1.0-5.0 Gyr		> 5.00 Gyr	
	tot	disk	tot	disk	tot	disk	tot	disk
A**	10	6	4	0	1	0	0	0
F**	0	0	1	0	17	2	5	0
G**	2	1	0	0	7	0	12	3
K**	3	2	2	0	5	0	12	0
total	15	9	7	0	30	2	29	3

Fig. 6 presents graphically the fraction of the (visual) stellar light reemitted in the infrared by the disk as a function of the stellar age. Similar diagrams based mainly on IRAS results, have been published before- see, for example, Holland et al. (1998). A general, continuous correlation appears: disks around PMS-stars (e.g. Herbig AeBe) are more massive than disks around stars like  $\beta$  Pic and Vega, and the disk around the Sun is still less massive. These earlier diagrams have almost no data on the age range shown in Fig. 6 and the new ISO data fill in an important hole.

Table 8 summarizes the detections at 60  $\mu$ m separately for stars of different age and of different spectral type together with the same numbers for stars with a disk; in the column marked “tot” the total number of stars (disks plus no-disks) is shown and under the heading “disk” the number of stars with a disk. The total count is 81 instead of 84 because for three of our target stars (two A-stars and one K-star) the age could not be estimated in a satisfying manner. Table 8 shows that the stars with a detected disk are systematically younger than the stars without disk: out of the 15 stars younger than 400 Myr nine (60%) have

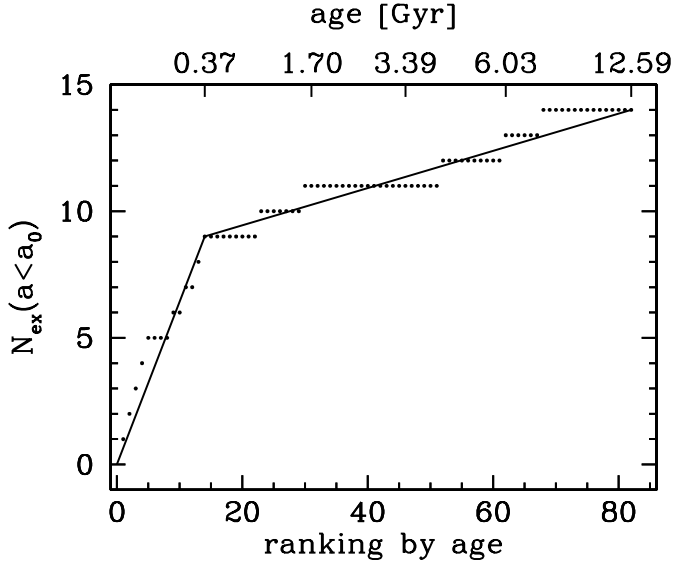


**Fig. 7.** Cumulative distribution of excess stars, as a function of the index after sorting by age. The two segments of a continuous straight line are predicted by assuming that in the first 400 Myr the rate of disappearance of disks is much higher than afterwards (see text).

a disk; out of the 66 older stars only five have a disk (8%). Furthermore, there exists a more or less sharply defined age above which a star has no longer a disk. This is best demonstrated by the A-stars. Six A-stars have a disk; the stellar ages are 220, 240, 280, 350, 360, 380 Myr. For the A-stars without disk the corresponding ages are 300, 320, 350, 380, 420, 480, 540, 890, 1230 Myr: 350 to 400 Myr is a well-defined transition region. We conclude that the A stars in general arrive on the main-sequence with a disk, but that they lose the disk within 50 Myr when they are about 350 Myr old.

Is what is true for the A-stars also valid for the stars of other spectral types? Our answer is “probably yes”: of the five F, G, and K stars younger than 400 Myr three (60%) have a disk. Of the 61 F, G, and K stars older than 400 Myr five have a disk (one in twelve or 8%). The percentages are the same as for the A-stars but the 60% for young G- and K-stars is based on only three detections. It seems that the disks around F, G, and K stars decay in a similarly short time after arrival on the main sequence.

An immediate question is: do *all* stars arrive at the main sequence with a disk? Studies of pre-main-sequence stars show that disks are common, but whether they always exist is unknown. The sequence of ages of the A-stars shows that the three youngest A-stars have a disk. This suggests that all stars arrive on the main sequence with a disk, but the suggestion is based on small-number statistics. We therefore leave the question without an answer but add two relevant remarks without further comment: some very young stars have no detectable disk, for example HD 116842 (A5V, 320 Myr), HD 20630 (G5V,

300 Myr), HD 37394 (K1V, 320 Myr) and some old stars have retained their disk; examples: HD 10700 (G8V, 7.2 Gyr), HD 75732 (G5V, 5.0 Gyr) and HD 207129 (G0V, 4.4 Gyr); the last case has been studied in detail (Jourdain de Muizon et al. 1999).

The age effect is shown graphically in Fig. 7; it displays the cumulative distribution of stars with a disk. The x-axis is the index of a star after all stars have been sorted by age. At a given age the local slope of the curve in this diagram gives the probability that stars of that age have a disk. The two line segments shows how the cumulative number increases when 70% of the disks disappear gradually in the first 0.4 Gyr and the remaining 30% gradually in the 12 Gyr thereafter.

In section 5.6 we will review the evidence that at about 400 Myr after the formation of the Sun a related phenomenon took place in the solar system.

### 5.5. The need to continuously replenish the dust particles

In “Vega-like” circumstellar disks the dust particles have a life-time much shorter than the age of the star. Within 1 Myr they will disappear via radiation pressure and the Poynting-Robertson effect (Aumann et al. 1984). An upper limit of  $10^6$  year is given for dust around A-type stars by Poynting-Robertson drag (Burns et al. 1979; Backman & Paresce 1993); the actual life time will be smaller: for  $\beta$  Pic, Artymowicz & Clampin (1997) find only 4000 years. Continuously new grains have to replace those that disappear. A plausible mechanism that can supply these new grains at a high enough rate and for a sufficient long time are the collisions between asteroids and planetesimals. Direct detection of such larger bodies is not yet possible although the existence of comets around  $\beta$  Pic is suggested by the rapidly appearing and disappearing components of the CaII K-absorption line (Ferlet et al. 1987). The total mass of the dust that ISO detected is about that of the Moon. To produce the dust for 400 Myr much more mass must be present in invisible form, that of asteroids or “planetesimals”. Thus the disappearance of the infrared excess on a timescale of 400 Myr does not trace the removal of the dust grains, but *the lifetime of the disk or planetesimals that replenishes the dust*. In the solar system the same may have happened; see below.

### 5.6. Disks in the presence of a companion star or a planet

When a star has a companion or a planet the gravitational field will have a time-variable component. Will this component destroy the disk? Not necessarily so: the planets Jupiter and Saturn have both a dust disk and many satellites.

On purpose we did not select narrow binaries: we rejected stars within 1 arcmin from a target star, unless this other star was at least 5 magnitudes fainter in the

*V*-band. This criterium accepts wide multiple-stars and indeed these occur. We used the Hipparcos Catalogue to check all 84 stars from Table 2 for multiplicity. Forty-eight stars have an entry in the “Catalogue of companions of double and multiple stars” (=CCDM), see Dommanget & Nys (1994). Among the 14 stars with a disk there are seven wide multiple-stars. In one case (HD22049) the star is part of an astrometric double; we ignore the object. That leaves us with six stars that have both a disk and stellar companions. The conclusion is therefore that companions do not necessarily destroy a disk.

Table 9 contains information on these six stars with both a disk and (at least) one companion. In column (1) the name appears, in column (2) the HD-number and in column (3) the entry-number in the CCDM; column (4) gives the total number of companions given in the CCDM, column (5) gives the distance,  $r$ , between A and B in astronomical units and column (6) the magnitude difference in the *V*-band between the first and the second component (“A” and “B”, respectively).

There are at least two remarkable cases in Table 9. One is Vega (HD 172167) with four companions; its brightest companion is at 490 AU, but its closest companion at only 200 AU, just outside of Vega’s disk. The other is  $\rho^1$  Cnc that has a disk (Dominik et al. 1998; Trilling & Brown 1998; Jayawardhana et al. 2000), a planet (Butler et al. 1997) and a stellar companion.

**Table 9.** Multiple systems with a dust disk

Name	HD	CCDM	$N_{\text{tot}}$	$r$	$\Delta m$
				AU	
$\tau$ Cet	10700	01441-1557	1	328	9.5
$\rho^1$ Cnc	75732	08526+2820	1	1100	7.2
$\beta$ Leo	102647	11490+1433	3	440	13.5
$\sigma$ Boo	128167	14347+2945	2	3700	5.3
$\alpha$ Lyr	172167	18369+3847	4	490	9.4
	207129	21483-4718	1	860	3.0

The data in Table 9 thus show that disks are found in wide multiple-systems: multiplicity does not necessarily destroy a disk.

### 5.7. The connection to the solar system

The solar system shows evidence for a fast removal of a disk of planetesimals a few hundred Myr after the Sun formed a disk. The best case is given by the surface of the Moon, where accurate crater counting from high resolution imaging can be combined with accurate age determinations of different parts of the Moon’s surface. The age of the lunar surface is known from the rocks brought back to earth by the Apollo missions; the early history of the Moon was marked by a much higher cratering rate than observed today; see for a discussion Shoemaker & Shoemaker (1999). This so-called “heavy bombardment”

lasted until some 600 Myr after the formation of the Sun. Thereafter the impact rate decreased exponentially with time constants between  $10^7$  and a few times  $10^8$  years (Chyba 1990).

Other planets and satellites with little erosion on their surface confirm this evidence: Mercury (Strom & Neukum 1988), Mars (Ash et al. 1996; Soderblom et al. 1974) Ganymede and Callisto (Shoemaker & Wolfe 1982; Neukum et al. 1997; Zahnle et al. 1998). The exact timescales are a matter of debate. Thus there are indications of a cleanup phase of a few hundred Myr throughout the solar system; these cleanup processes may be dynamically connected.

## 6. Conclusions on the incidence of remnant disks

The photometers on ISO have been used to measure the 60 and  $170\mu\text{m}$  flux densities of a sample of 84 main-sequence stars with spectral types from A to K.

On the basis of the evidence presented we draw the following conclusions:

- Fourteen stars have a flux in excess of the expected photospheric flux. We conclude that each of these has a circumstellar disk that is a remnant from its pre-main-sequence time. Two more stars may have a disk, but there is a significant chance that the emission is due to a background galaxy.
- The overall incidence of disks is 14/84 or 17%. A-stars have a higher incidence than the other stars.
- We prove that the detectability of a given disk is the same for A, F and G-stars with the same photospheric flux at  $60\mu\text{m}$ ; K stars have a lower probability of detection.
- The disks that we detect have a value of  $\tau$ , between  $2 \times 10^{-4}$  and  $4 \times 10^{-6}$ . The upper limit is real: main-sequence stars do not carry stronger disks; the exception is  $\beta$  Pic with  $\tau = 8 \times 10^{-3}$ . The lower limit is caused by selection effects: fainter disks are below our detection threshold.
- Six out of the ten A-type stars younger than 400 Myr have a disk; the disk is absent around all five older A-type stars: the disks disappear around this age.
- Disks around F-, G- and K-stars probably disappear on a similar time scale. The disappearance of disks is *not* a continuous process; 400 Myr is the age at which most disks disappear.
- In the history of our solar system the abrupt ending of the initial “heavy bombardment” of the Moon has the same time scale.
- We suggest that the disks that we detect are actually sites where a “heavy bombardment” takes place now. The time scale on which the disks disappear is actually the time scale of the disappearance of the bombarding planetesimals.
- The mass that we detect through its infrared emission is only a minute fraction (about  $10^{-5}$ ) of the mass

present. We see the gravel but not the very big stones that produce it.

- Some very young stars lack a disk; some very old stars still have a disk: the existence of both groups needs to be explained.
- Stars in multiple systems retain their remnant disks as often as isolated stars.

*Acknowledgements.* The ISOPHOT data presented in this paper was reduced using PIA, which is a joint development by the ESA Astrophysics Division and the ISOPHOT consortium. In particular, we would like to thank Carlos Gabriel for his help with PIA. We also thank J. Dommangé for helpful information on the multiplicity of our stars and the referee, R. Liseau for his careful comments. This research has made use of the Simbad database, operated at CDS, Strasbourg, France, and of NASA’s Astrophysics Data System Abstract Service. CD was supported by the Stichting Astronomisch Onderzoek in Nederland, Astron project 781-76-015.

## References

Ábrahám P., Leinert C., Burkert A., Lemke D., Henning T., 1998, A&A 338, 91  
 Artymowicz P., Clampin M., 1997, ApJ 490, 863  
 Artymowicz P., Burrows C., Paresce F., 1989, ApJ 337, 494  
 Ash R.D., Knott S.F., Turner G., 1996, Nature 380, 57  
 Aumann H., 1985, PASP 97, 885  
 Aumann H., Gillett F., Beichman C., et al., 1984, Ap.J. 278, L23  
 Backman D., Paresce F., 1993, in Levy E., Lunine J., eds., Protostars and Planets III, pp. 208–2000, University of Arizona, Tucson  
 Beckwith S., Sargent A., 1996, Nature 383  
 Blieck N.v.d., Prusti T., Waters L., 1994, A&A 285  
 Burns J.A., Lamy P.L., Soter S., 1979, Icarus 40, 1  
 Butler R., Marcy E. G.W. and Williams, Hauser H., Shirts P., 1997, ApJLet 474, L115  
 Chini R., Kruegel E., Kreysa E., Shustov B., Tutukov A., 1991, A&A252, 220  
 Chyba C.F., 1990, Nature 343, 129  
 Dent W., Walker H., Holland W., Greaves J., 2000, MNRAS 314, 702  
 Dole H., Gispert R., Lagache J.L. Guilaine Puget, et al., 2000, in Lemke D., Stickel M., Wilke K., eds., ISO Surveys of a Dusty Universe, Springer Verlag, (astro-ph/0002283)  
 Dominik C., Laureijs R., Jourdain de Muizon M., Habing H., 1998, A&A 329, L53  
 Dommangé J., Nys O., 1994, Comm. Obs. R. Belgique, Ser. A. 115  
 Draine B., Lee H., 1984, ApJ 285, 89  
 Elbaz D., Cesarsky C., Fadda D., et al., 2000, A&A Lett in press, (astro-ph/9910406)  
 Ferlet R., Hobbs L., Vidal-Madjar A., 1987, A& A 185, 267

Gillett F., 1986, in Israel F., ed., *Light on dark matter*, pp. 61–70, Reidel, Dordrecht

Habing H., Bouchet P., Dominik C., et al., 1996, *A&A* 315, L233

Habing H., Dominik C., Jourdain de Muizon M., et al., 1999, *Nature* 401, 456–458

Hobbs L., Vidal-Madjar A., Ferlet R., Albert C., Gry R., 1985, *ApJLet* 293, L29

Holland W., Greaves J., Zuckerman B., et al., 1998, *Nature* 392, 788

Jayawardhana R., Holland W., Greaves J., et al., 2000, *ApJ* 536, 425

Johnson H., Wright C., 1983, *ApJS* 53, 643

Jourdain de Muizon M., Laureijs R., Dominik C., et al., 1999, *A&A* 350, 875

Kamp I., Bertoldi F., 2000, *A&A* 353, 276

Kessler M., Steinz J., Anderegg M., et al., 1996, *A&A* 315, L27

Klaas U., Krüger H., Heinrichsen I., Heske A., Laureijs R., 1994, *ISOPHOT Observer's Manual, Version 3.1*, ESA Publication

Kunzli M., North P., Kurucz R.L., Nicolet B., 1997, *A&AS* 122, 51

Lachaume R., Dominik C., Lanz T., Habing H., 1999, *A&A* 348, 897

Laureijs R., Klaas U., Richards P., Schulz B., 2000, *ISO Handbook, Volume V: PHT-The Imaging Photo-Polarimeter version 1.0*, ISO Data Centre, (url: [www.iso.vilspa.esa.es/manuals/HANDBOOK/V/](http://www.iso.vilspa.esa.es/manuals/HANDBOOK/V/))

Lemke D., Klaas U., Abolins J., et al., 1996, *A&A* 315, L64

Liseau R., 1999, *A&A* 348, 133

Mannings V., Barlow M., 1998, *ApJ* 497, 330

Matsuura H., Kawara K., Sato Y., et al., 2000, *A&A* accepted, (astro-ph/0006444)

Natta A., Panagia N., 1976, *A&A* 50, 191

Neukum G., Wagner R., Wolf U., et al., 1997, *BAAS* 29, 984

Oliver S., Serjeant S., Efstatihou A., et al., 2000, in Lemke D., Stickel M., Wilke K., eds., *ISO Surveys of a Dusty Universe*, Springer Verlag, (astro-ph/0005279)

Perryman M., O'Flaherty K., van Leeuwen F., et al., 1997, *The Hipparcos and Tycho Catalogues*, ESA SP-1200

Plets H., Vynckier C., 1999, *A&A* 343

Plets H., Waelkens C., Oudmaijer R., Waters L., 1997, *A&A* 323, 513

Sargent A., Welch W., 1993, *Annu. Rev. Astron. Astrophys.* 31, 297

Shoemaker E., Shoemaker C., 1999, in Beatty J.K., Petersen C., Chaikin A., eds., *The new solar system*, 4th edition, pp. 69–85, Sky Publishing Corporation and Cambridge University Press

Shoemaker E.M., Wolfe R.A., 1982, in Morrison D., ed., *Satellites of Jupiter*, pp. 277–339, Univ. of Arizona Press, Tucson

Smith B., Terrell R., 1984, *Science* 226, 1421

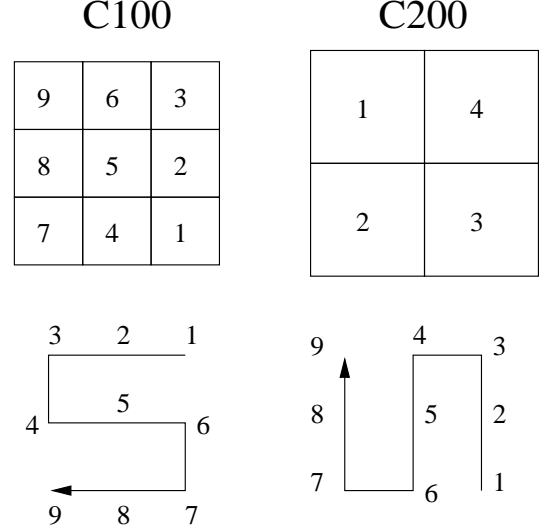


**Fig. A.1.** The upper half labels the different pixels of the C100 and C200 detectors seen in projection on the sky. The lower half describes the stepping directions: see text.

Soderblom L.A., Condit C.D., West R.A., Herman B.M., Kreidler T.J., 1974, *Icarus* 22, 239

Strom R.G., Neukum G., 1988, in *Mercury*, pp. 336–373, University of Arizona Press

Trilling D., Brown R., 1998, *Nature* 395, 775

van Dishoeck E., Blake G.A., 1998, *Annu. Rev. Astron. Astrophys.* pp. 317–368

Walker H., Wolstencroft R., 1988, *PASP* 100, 1509

Waters L., Coté J., Aumann H., 1987, *Astronomy and Astrophysics* 172, 225

Weissman P.R., 1984, *Science* 224, 987

Woolley R., Epps E., Penston M., Pocock S., 1970, *Royal Obs. Ann.* 5

Zahnle K., Dones L., Levison H.F., 1998, *Icarus* 136, 202

Zuckerman B., Becklin E.E., 1993, *ApJ* 414, 793

## Appendix A: Observing strategy for minimaps

The observations at 60  $\mu\text{m}$  and 170  $\mu\text{m}$  have been taken as minimaps with the C100 and C200 detector arrays using 3x3 rastersteps ; see Fig. A.1. In this figure the upper half shows the labeling, “ $p$ ”, of the 9, respectively 4 pixels (detectors) for the C100 and C200 arrays. The lower diagram gives the numbering, “ $r$ ”, of the successive array positions as it moves over the sky; the raster step is 46 arcseconds for both arrays. Consider first a measurement with the C100 array. At raster step  $r = 1$  the source illuminates pixel  $p = 7$ ; at the next step,  $r = 2$ , the source illuminates  $p = 4$ , at  $r = 3$  the source is on  $p = 1$ , etc.. For the C200 measurements  $r = 1$  has the source on  $p = 1$ ; at  $r = 2$  the source is half on  $p = 1$  and half on  $p = 2$ ; at  $r = 3$  the source is on  $p = 2$ , et cetera.

**Table B.1.** Weight factors for minimap flux determination

Pix	Raster position								
	1	2	3	4	5	6	7	8	9
C100									
1	0	0	1	0	0	( $-\frac{1}{3}$ )	$-\frac{1}{3}$	$-\frac{1}{3}$	0
2	$-\frac{1}{3}$	0	0	1	0	( $-\frac{1}{3}$ )	$-\frac{1}{3}$	0	0
3	$-\frac{1}{3}$	$-\frac{1}{3}$	0	0	0	( $-\frac{1}{3}$ )	0	0	1
4	0	1	0	0	0	(0)	$-\frac{1}{3}$	$-\frac{1}{3}$	$-\frac{1}{3}$
5	$-\frac{1}{4}$	0	$-\frac{1}{4}$	0	1	(0)	$-\frac{1}{4}$	0	$-\frac{1}{4}$
6	$-\frac{1}{3}$	$-\frac{1}{3}$	$-\frac{1}{3}$	0	0	(0)	0	1	0
7	1	0	0	$-\frac{1}{3}$	0	(0)	0	$-\frac{1}{3}$	$-\frac{1}{3}$
8	0	0	$-\frac{1}{3}$	$-\frac{1}{3}$	0	(1)	0	0	$-\frac{1}{3}$
9	0	$-\frac{1}{3}$	$-\frac{1}{3}$	$-\frac{1}{3}$	0	(0)	1	0	0
C200									
1	1	0	0	0	0	0	0	0	-1
2	0	0	1	0	0	0	-1	0	0
3	-1	0	0	0	0	0	0	0	1
4	0	0	-1	0	0	0	1	0	0

## Appendix B: Data reduction

We used the following procedure to extract the flux. The result of a minimap measurement is a flux per pixel for each pixel and each raster position. Let  $f(p, r)$  be the measured flux in pixel  $p$  at raster position  $r$ . There are  $n_p$  pixels and  $n_r$  raster positions. We first calculate a flat field correction  $f_{\text{flat}}(p)$  for each pixel by assuming that at one raster position the flux averaged over all pixels is the same

$$f_{\text{flat}}(p) = \frac{\frac{1}{n_p} \sum_{p'=1}^{n_p} \sum_{r'=1}^{n_r} f(p', r')}{\sum_{r'=1}^{n_r} f(p, r')} \quad (\text{B.1})$$

Since the individual pixels in the C100/C200 cameras have different properties, we use the measurements of each pixel to derive a separate measurement of the source flux. In order to compute the background-subtracted source flux, we assign to each raster position a weight factor  $g(p, r)$ . Since the exact point spread function is not known well enough, we use as on-source measurement the raster position where the pixel was centered on the source (weight factor 1). The background measurement is derived by averaging over the raster positions where the same pixel  $p$  was far away from the source (weight  $-1/3$  or  $-1/4$ ). Raster positions in which the pixel was partially on the source are ignored (weight 0). The resulting weight factors are given in Table B.1. The source flux measured by pixel  $p$  is given by

$$F(p) = \frac{f_{\text{flat}}}{f_{\text{psf}}} \sum_{r'=1}^{n_r} g(p, r') f(p, r') \quad (\text{B.2})$$

$f_{\text{psf}}$  is the point spread function correction factor as given by Laureijs et al. (2000). We then derive the flux  $F$  and the error  $\sigma$  by treating the different  $F(p)$  as independent measurements.

$$F = \frac{1}{n_p} F(p) \quad (\text{B.3})$$

$$\sigma = \frac{1}{\sqrt{n_p - 1}} \sqrt{\sum_{p'=1}^{n_p} (F(p') - F)^2} \quad (\text{B.4})$$

The point spread function is broader than a pixel. We have corrected for this, using the parameter  $f_{\text{psf}}$  given above. The correction factor may be too low: Dent et al. (2000) show that the disk around Fomalhaut ( $\alpha$  PsA) is extended compared to our point-spread function. This means that all our 60  $\mu\text{m}$  and 170  $\mu\text{m}$  detections are probably somewhat underestimated.

We have ignored pixel 6 of the C100 camera entirely, because its characteristics differ significantly from those of the other pixels: it has a much higher dark signal and anomalous transient behaviour.

In the future the characteristics of each pixel will be determined with increasing accuracy. It may prove worthwhile to redetermine the fluxes again.

## Appendix C: Optical depth of the disk, detection limit and illumination bias

We discuss how the contrast factor,  $C_{60}$ , depends on the spectral type of the star,  $T_{\text{eff}}$ , and on the optical depth,  $\tau$ , of the disk. The dust grains in the remnant disk are relatively large, at least in cases where a determination of the grain size has been possible (Bliek et al. 1994; Artymowicz et al. 1989) and the absorption efficiency for stellar radiation will be high for stars of all spectral types. The efficiency for emission is low: the dust particles emit beyond 30  $\mu\text{m}$  and these wavelengths are larger than that of the particles. We assume that the dust grains are all of a single size,  $a$ , and located at a single distance,  $r$ , from the star. We will introduce various constants that we will call  $A_i$ ,  $i = 0 - 6$ .

$$C_{60} \equiv \frac{L_{\nu, \text{d}}}{L_{\nu, *}} = \frac{L_{\nu, \text{d}}}{L_d} \cdot \frac{L_d}{L_*} \cdot \frac{L_*}{L_{\nu, *}}. \quad (\text{C.1})$$

First we determine  $L_{\nu, \text{d}}$ , the luminosity of the disk at the frequency  $\nu$ , and  $L_d$ , the total luminosity of the disk:

$$L_{\nu, \text{d}} = N 4\pi^2 a^2 Q_\nu B_\nu(T_d) \quad (\text{C.2})$$

and

$$L_d = N 4\pi^2 a^2 \int_0^\infty Q_\nu B_\nu(T_d) d\nu. \quad (\text{C.3})$$

We consider dust emission at  $60\ \mu\text{m}$ ;  $B_\nu(T)$  can be approximated by the Wien-equation. We thus write:

$$L_{\nu,d} = A_0 \exp\left(-\frac{240\ K}{T_d}\right) \quad (\text{C.4})$$

Define the average absorption efficiency:

$$Q_{\text{ave}}(T_d) \equiv \pi \int_0^\infty Q_\nu B_\nu(T_d) d\nu / (\sigma T_d^4). \quad (\text{C.5})$$

For low dust-temperatures  $Q_{\text{ave}}$  can be approximated by  $Q_{\text{ave}} = A_1 T_d^\alpha$  with  $\alpha \approx 2$  (Natta & Panagia 1976) and thus

$$L_d = A_2 T_d^6. \quad (\text{C.6})$$

Second, we determine the stellar luminosity,  $L_{\nu,*}$ , at frequency  $\nu$  and the total stellar luminosity,  $L_*$ , both by ignoring the effects of dust, that is the luminosity at the photospheric level. The photospheric emission is approximated by the Rayleigh-Jeans equation:

$$L_{\nu,*} = \frac{\pi B_\nu(T_{\text{eff}})}{\sigma T_{\text{eff}}^4} L_* = \frac{A_3 L_*}{T_{\text{eff}}^3} \quad (\text{C.7})$$

The stellar luminosity for main sequence stars of spectral type A0–K5 can be approximated within 30% by:

$$L_* = A_4 T_{\text{eff}}^{8.2} \quad (\text{C.8})$$

Third, we determine the relation between  $T_d$  and  $T_{\text{eff}}$ . For photospheric temperatures  $Q_{\text{ave}}$  is independent of  $T_{\text{eff}}$ . The energy absorbed by a grain is thus  $\propto L_* \propto T_{\text{eff}}^{8.2}$ . The energy emitted is  $\propto T_d^6$ . Because the energy emitted equals the energy absorbed we conclude that  $T_{\text{eff}} = A_5 T_d^{6/8.2}$ .

Combining these results we find

$$C_{60} = A_6 \cdot \frac{1}{T_d^{3.8}} \cdot \exp\left(-\frac{240}{T_d}\right). \quad (\text{C.9})$$

We have calculated  $C_{60}$  without making the various approximations in Eqs. C.1 through C.7: Fig. C.1 shows the results. The results are valid if the distance dust-ring/star is the same (50 AU) for all stars irrespective of the spectral type.

In the figure we assume that for an A0-star  $C_{60}$  has the value 1 and  $T_d = 80$  or  $120\ K$ . For a star of later spectral type, the dust will be cooler and will emit less energy (see Eq. C.6), but since  $\lambda = 60\ \mu\text{m}$  is at the Wien-side of the black body curve, the emission at  $60\ \mu\text{m}$  will increase- see Eq. C.4. The consequence is that  $C_{60}$  remains constant for A-, F- and early G-type stars. For late G- and for K- and M-type stars the dust becomes too cold to be detected at  $60\ \mu\text{m}$ . Only photometry at longer wavelengths will ultimately be able to detect such very cold disks.

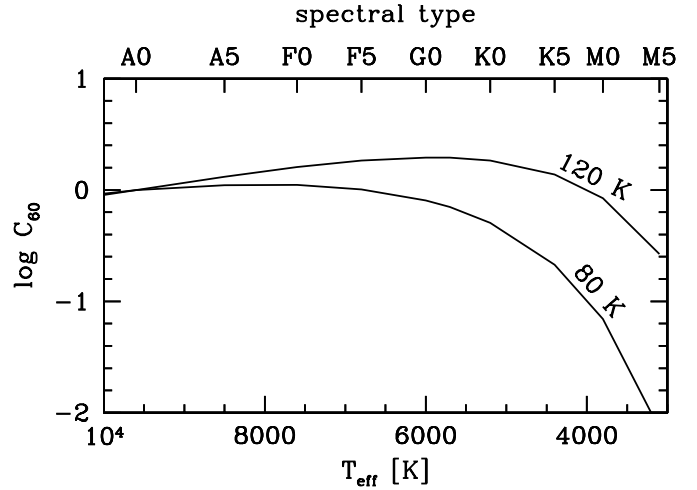


**Fig. C.1.** The contrast factor  $C_{60} \equiv F_\nu^d / F_\nu^{\text{pred}}$  for a ring of dust at a distance of 50 AU from the star and for stars of different effective temperature. We assumed  $T_d$  to be 80 or 120 K for an A0 star.

#### Appendix D: Determination of $\tau$ from observed fluxes

For most of our stars we have only a detection of the disk at  $60\ \mu\text{m}$ . To calculate the optical depth and the mass of the disk we need an estimate of the disk emission integrated over all wavelengths. If the dust around an A star has a temperature of  $T_d$ , the stars of later types will have lower dust temperatures. Numerical evaluation shows that, assuming constant distance between the star and the dust, the following relation is a good approximation

$$T_d = \dot{T}_d - \frac{\dot{T}_d}{\dot{T}_* - 2000} (\dot{T}_* - T_*) \quad . \quad (\text{D.1})$$

With this estimate of the dust temperature, a single flux determination is sufficient to determine the the fractional luminosity. We have used this method to determine estimates of  $\tau$  independently from all wavelength where we have determined an excess. We used  $\dot{T}_* = 9600\ K$  and  $\dot{T}_d = 80\ K$ , values that agree with those measured for Vega.